Joule

CellPress

Article

Understanding Full-Cell Evolution and Non-chemical Electrode Crosstalk of Li-Ion Batteries

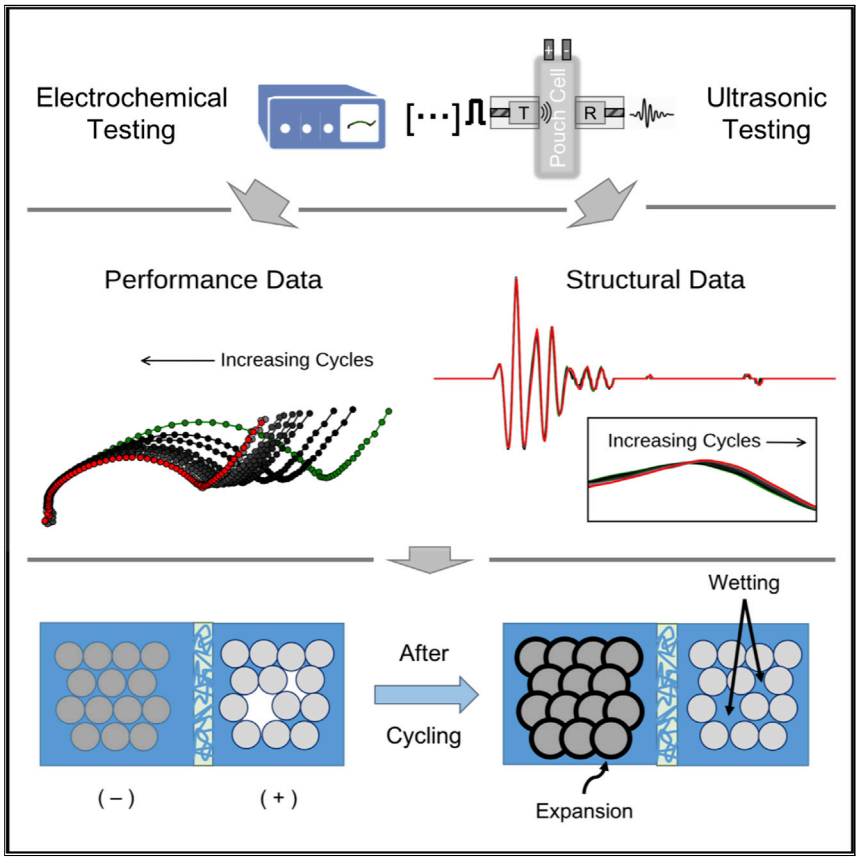

This study investigates the evolution of material and electrochemical properties in commercial lithium-ion batteries during cycling. Results indicate that as-received batteries undergo a post-formation break-in period, which is signified by an initial, rapid evolution of the battery's properties before stabilizing. Break-in corresponds to non-chemical crosstalk, whereby physical changes in the negative electrode affect the electrochemical performance of the positive electrode. These findings demonstrate how interplay between components during early cycles can affect the future battery performance.

Kevin W. Knehr, Thomas Hodson, Clement Bommier, Greg Davies, Andrew Kim, Daniel A. Steingart

steingart@princeton.edu

HIGHLIGHTS

Evolution of commercial Li-ion batteries during cycling was studied

A post-formation "break-in" period during the first few cycles was identified

Ultrasonic methods captured changes in material properties of graphite electrode

Non-chemical crosstalk between electrodes reduced cell impedance during break-in

Knehr et al., Joule 2, 1146–1159
June 20, 2018 © 2018 Elsevier Inc.
https://doi.org/10.1016/j.joule.2018.03.016

Joule

CellPress

Article

Understanding Full-Cell Evolution and Non-chemical Electrode Crosstalk of Li-Ion Batteries

Kevin W. Knehr,[1,2,5] Thomas Hodson,[1,2,5] Clement Bommier,[1,2] Greg Davies,[1,2] Andrew Kim,[2,3] and Daniel A. Steingart[1,2,4,6,*]

SUMMARY

The confined, sealed design of a commercial lithium-ion battery makes it difficult to probe and understand how the system evolves during cycling. In this work, we investigate the full-cell evolution of lithium-ion batteries using two complementary techniques, electrochemical impedance spectroscopy (EIS) and ultrasonic time-of-flight analysis, which make it possible to couple electrochemical and material property changes during cycling. It is found that there is a post-formation "break-in" period before full-cell behavior stabilizes. This period is signified by an increased swelling of the graphite anode, likely caused by side reactions, which increases the pressure within the cell. The increased pressure forces electrolyte to wet previously inactive portions of the lithium cobalt oxide cathode, lowering the cell impedance. The results demonstrate how the full-cell performance can be greatly affected by non-chemical crosstalk between the two electrodes and indicates the importance of using multiple complementary experimental techniques.

INTRODUCTION

Lithium-ion batteries have become ubiquitous in modern life, with almost universal adoption in the consumer electronics and burgeoning electric vehicle markets. Specifically, electric vehicle applications require constant, reliable battery performance in order for the vehicles to maintain a commercially competitive range throughout their life. However, irregularities in battery performance, even under the same cycling protocols, make predicting usable cycle life of lithium-ion batteries difficult.[1–6]

For instance, Harris et al. have recently shown that the performance of lithium-ion batteries varies widely, with nominally identical cells reaching 80% of their initial capacity anywhere from 250 to 600 cycles.[6] One of the main reasons for the large spread in cycle life is an incomplete understanding of how and why the electrochemical and physical properties of a battery evolve during operation. This incomplete understanding makes it difficult to design battery systems that account for such property evolutions.

Recent efforts at understanding the evolution of lithium-ion batteries have primarily focused on identifying a single feature of the battery and characterizing how it changes during cycle life. Often, the overall goal is to determine whether this unique feature can be used as a metric for predicting remaining cycle life, with little focus on understanding the physical processes responsible for the change. Studies have focused on diagnosing changes in the charge/discharge performance,[7–9] the

Context & Scale

Batteries designed for electric vehicles must be able to provide constant, reliable performance for 10–15 years. Variations in performance at any point in a battery's life make it difficult for vehicle manufacturers to provide accurate diagnostics (e.g., remaining range and required charge time). In this work, we show that as-received batteries, which have already undergone a cycling protocol from the manufacturer (known as the formation process), can still undergo a post-formation break-in period. The break-in period is signified by an initial, rapid evolution of the physical and electrochemical properties before reaching stable values. This work demonstrates that, even after an initial cycling protocol, periods of rapid property change can still exist in a battery. Such periods could be important for understanding how electric vehicles operate after transition points in their use (i.e., after long periods of disuse or changes in the use profile).

electrochemical resistances,[10–16] the size of the battery,[17–22] and the stresses within the battery.[23–28]

While existing studies have provided useful information about the progression of battery properties during cycling, questions still remain as to the root cause of capacity variation as a function of operation. In addition, they often fail to address an important question associated with battery reliability: is it possible to detect early on when a battery will fail? In this work we have found that there is an important period between "formation" and "steady state," which we call "break-in." It is widely accepted "lab lore" that the first few cycles of a battery, post formation, are different from the behavior the battery exhibits at steady state.[9,24] Beyond this, the break-in period may be better described as a viscoelastically limited transient that indicates a new timescale of battery behavior, as shown later. Understanding and controlling break-in conditions could determine future performance of the cell. In this work, we take the first step toward testing this hypothesis by proposing an explanation for the physical and electrochemical changes occurring in a battery during the post-formation break-in period.

To accomplish this, we implement two complementary techniques: electrochemical impedance spectroscopy (EIS) to study changes in the electrochemical resistances, and ultrasonic time-of-flight (ToF) analysis to study changes in the physical properties of the battery. While EIS is a common electrochemical characterization technique, ultrasonic ToF analysis is a new tool capable of probing the changes in material properties by measuring changes in the amplitude and ToF of ultrasonic waves passing through the battery.[29–32] The technique is a non-destructive, non-invasive tool capable of monitoring changes in the physical properties of the battery in real time. The goal of this study is to combine ultrasonic ToF analysis with EIS to elucidate the structure/performance relationship in the battery during break-in.

RESULTS AND DISCUSSION

Observable Correlations in EIS and Ultrasonic Data

Examples of the raw data from the EIS and ultrasonic measurements are shown in Figure 1 for a graphite/lithium cobalt oxide (LCO) pouch cell. Figures 1A and 1B show the Nyquist plots obtained from the EIS experiments at the start and end of discharge, respectively, during the first 50 cycles. Figures 1C and 1D show the raw ultrasonic waveforms at the start and end of discharge, respectively. The waveforms were generated by pulsing a transducer on one face of the battery and recording the ultrasonic signal on the transverse face (see Experimental Procedures for details). The insets in Figures 1C and 1D are magnifications of the third peak in the ultrasonic data, showing the shift in signal.

The same trend is observed in both sets of data (start and end of discharge), whereby the semicircle of the EIS data decreases and the ToF of the ultrasonic signal increases with increasing cycles. This suggests that the temporal changes in the electrochemical response of the battery and the ultrasonic signal through the battery may be coupled.

EIS Shows Decrease in LCO Charge Transfer Resistance

To further elucidate the observed correlations, we analyzed the EIS data by fitting the experimental data to the equivalent circuit model proposed by Zhang et al.[33] A diagram of the equivalent circuit model is shown in Figure S2 along with a description of how the model applies to the experimental data. The largest change in the EIS data in Figure 1 is a decrease in the radius of the large semicircle as the cell is cycled, which corresponds to a decrease in the charge transfer resistance (R_{CT}).

[1]Department of Mechanical and Aerospace Engineering & Andlinger Center for Energy and the Environment, Princeton University, Princeton, NJ 08544, USA

[2]Andlinger Center for Energy and the Environment, Princeton University, Princeton, NJ 08554, USA

[3]Department of Electrical Engineering, Princeton University, Princeton, NJ 08544, USA

[4]Department of Chemical and Biological Engineering, Princeton University, Princeton, NJ 08544, USA

[5]These authors contributed equally

[6]Lead Contact

*Correspondence: steingart@princeton.edu

https://doi.org/10.1016/j.joule.2018.03.016

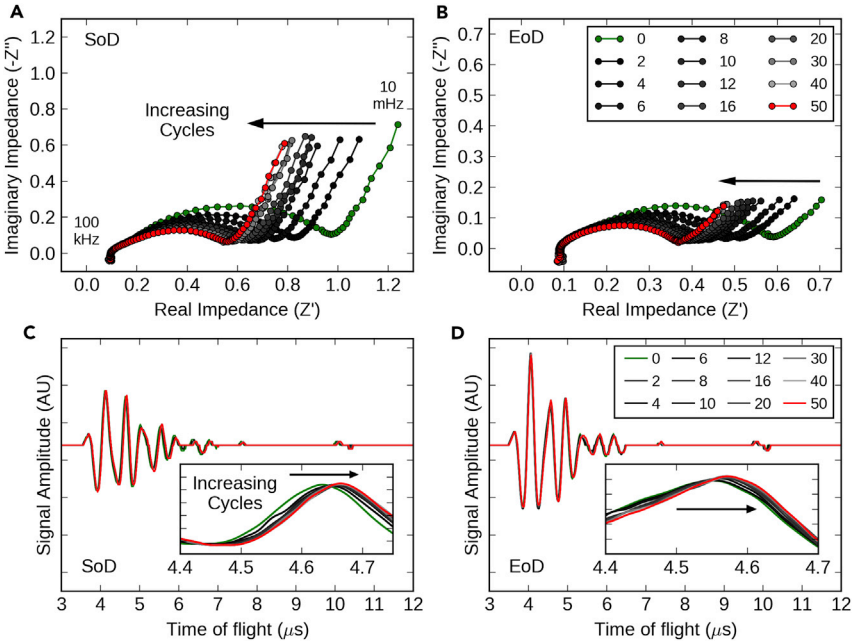

Figure 1. Correlations in EIS and Ultrasonic Data

(A) Nyquist plot at the start of discharge obtained from electrochemical impedance spectroscopy for a 210 mAh LCO pouch cell cycled at C/2 between 2.7 and 4.2 V with a constant voltage charge step at 4.2 V to a C/20 cutoff current.

(B) Nyquist plot at the end of discharge for same experiment.

(C) Transmitted ultrasonic signals at start of discharge obtained simultaneously from same cells. Insets: zoom-in of ultrasonic data showing shifts in signals.

(D) Transmitted ultrasonic signals at the end of discharge for the same experiment.

All data were obtained after 2 hours of rest. The green data were recorded at the start of cycling and the red data were recorded at cycle 50 (color online).

Several authors have deconvoluted R_{CT} to obtain separate resistances for the reactions at the graphite anode (R_a) and LCO cathode (R_c)[13,14,34–37]. In this work, we attempt to attribute the contribution of each electrode to the overall R_{CT} by conducting EIS experiments on symmetric coin cells. The resulting Nyquist plots for the cathode/cathode and anode/anode cells are shown in Figure S3. The cells composed of LCO have a much larger R_{CT}, indicating that the R_{CT} of the full pouch cell can mainly be attributed to the reaction on the LCO. This result is in agreement with previous studies in the literature on LCO batteries.[12,38–41] It suggests that the R_{CT} of the pouch cell decreases with cycling because the insertion and deinsertion into the LCO is becoming easier.

R_{CT} and ToF Shift Highlight Break-In Phenomenon

Figure 2 provides a more quantitative description of the results in EIS and ultrasonic measurements during the initial cycling of the LCO cell. Figures 2A and 2B contain the R_{CT} obtained from the equivalent circuit fit and the ToF shift of the ultrasonic signal, respectively, during the first 100 cycles. The EIS and ultrasonic data show similar trends, whereby the values rapidly change during the initial 12 cycles, which is referred to herein as the break-in period, and then level off. In Figure 2A, the open triangles represent a cell that was operated under the same conditions with fewer periodic EIS measurements. The agreement between both cells indicates that the trend in R_{CT} is reproducible. Reproducible behaviors between cells were also observed for the ultrasonic ToF data, but for brevity these data were omitted.

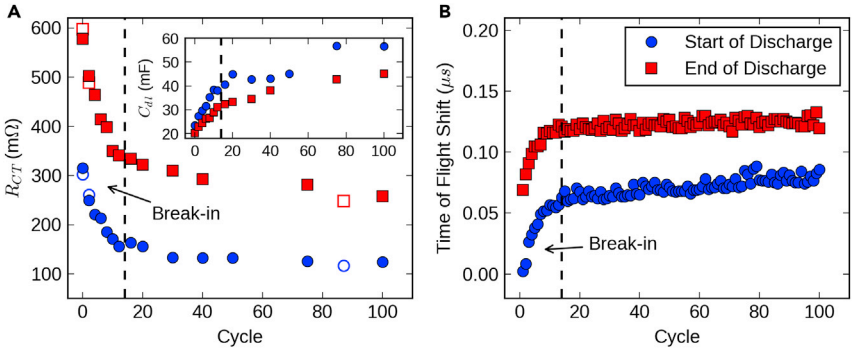

Figure 2. Break-In Period Identified by Changes in R_{CT} and ToF Shift

(A) Charge transfer resistance from EIS experiments during the first 100 cycles of an LCO pouch cell cycled between 2.7 and 4.2 V. Data were taken after a 2-hr rest for cycles 0, 2, 4, 6, 8, 10, 12, 16, 20, 30, 40, 50, 75, and 100. The open symbols were obtained from a separate cell cycled under the same conditions, but with EIS taken during cycles 0, 2, and 87. Inset: capacitive double layer over 100 cycles obtained from equivalent circuit fit of EIS data.

(B) ToF shift from ultrasonic signals taken every cycle, whereby the shift in signal was calculated in reference to the start of discharge of cycle 0.

Note that this behavior may be a universal feature of lithium-ion pouch-cell batteries. For instance, similar behavior in R_{CT} and ToF shift is observed for LCO batteries from separate suppliers (Figure S4). In addition, batteries containing graphite/lithium iron phosphate electrodes show similar trends (Figure S5). For the remainder of this paper, we will attempt to elucidate the cause of this behavior through an in-depth analysis of the initial LCO cells.

In Figure 2A, the R_{CT} measured at the end of discharge (EoD) is consistently higher than at the start of discharge (SoD). This has previously been attributed to an increase in the charge transfer resistance of the LCO with increased lithiation.[42,43] Interestingly, the R_{CT} measured at SoD and EoD both decrease by ~40% during the initial 12 cycles. R_{CT} can decrease in two ways: (1) an improvement in the reaction kinetics and (2) an increase in the surface area available for reaction. The inset in Figure 2A suggests that the resistance is decreasing because of an increase in surface area. The inset shows the double-layer capacitance (C_{dl}) obtained from the equivalent circuit fit. C_{dl} increases rapidly during the break-in period, then appears to level off at later cycles. Because the double-layer capacitance only depends on surface area, this result indicates that an increase in the active area is responsible for the observed trends in the EIS data. More specifically, the active area of the LCO is increasing, as suggested by the analysis in the previous section.

Along with an abrupt decrease in R_{CT}, the break-in period corresponds to an abrupt increase in the ToF shift of the ultrasonic signal, as indicated in Figure 2B. During the first 12 cycles, the ToF increases by ~60 ns at both SoD and EoD. The changes in the ultrasonic signal that produces the ToF increase could result from changes in wave attenuation. Changing attenuation leads to changes in wave dispersion (waves traveling at different velocities), which may affect measured ToF shifts. To test whether attenuation is a factor, we recalculated the ToF shifts using narrowly filtered frequency ranges of the ultrasonic signals. If all frequency components of the ultrasonic signal shift in the same manner with respect to cycling, changes in attenuation of the signals are negligible factors. Figure S6 shows the raw ultrasonic signal (Figures S6A–S6C), the ~2.0 MHz contribution to the signal (Figures S6D–S6F), and the

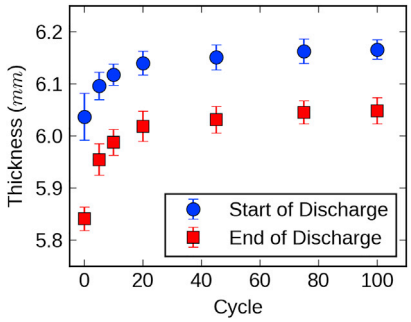

Figure 3. Change in Cell Thickness During Cycling

Measured average thickness change of three LCO pouch cells cycled between 2.7 and 4.2 V at the start and end of discharge. Error bars refer to spread from the three batteries.

~3.2-MHz contribution to the signal (Figures S6G–S6I). All parts of the signal produce similar ToF shifts, indicating that changes in the ToF are caused by shifts in the full ultrasonic waveform and not by changes in the attenuation of the wave. Since changes in attenuation of the signal are negligible, two remaining factors may cause the increase in the ToF of the signal: (1) an increase in the thickness of the battery and (2) a decrease in the effective sound speed of the ultrasonic wave.

ToF Shifts from Battery Swelling and Decreasing Effective Modulus

Cell-level dilation can cause a change in ToF. To account for this we measured the thickness of three LCO pouch cells during cycling, and the results of these measurements are shown in Figure 3, which reports the average thickness with the error bars referring to the spread from the three batteries.

Note that the thickness measurements show the batteries decreasing in size within a given cycle from SoD to EoD. This is in contrast to an increase in the ToF of the signal from SoD to EoD shown in Figure 2B. This behavior is attributed to a decrease in the effective modulus of the graphite electrode during discharge, which slows the speed of the ultrasonic wave.[32]

In terms of cycle life, the data in Figure 3 show that the average thickness of the cells increases by >100 μm over the first 100 cycles at both SoD and EoD. The battery swelling can be attributed to the expansion of the graphite anode.[17,18,44] The expected increase in ToF shift due to the increase in cell thickness can be calculated using the following equation:

$$t_{wave} = \frac{l}{c_s}, \qquad \text{(Equation 1)}$$

where t_{wave} is the time it takes an ultrasonic wave to traverse the battery, l is the thickness of the battery, and c_s is the effective speed of sound, which is defined as

$$c_s = \left(\frac{E_{eff}}{\rho}\right)^{0.5}, \text{ where } \rho = \frac{m}{Al}. \qquad \text{(Equation 2)}$$

In Equation 2, E_{eff} and ρ are the effective modulus and density of the battery, respectively, m is the battery mass, and A is the battery area. Note that describing the ultrasonic velocity using Equation 2 is only valid if the ultrasonic wavelength is significantly larger than the inhomogeneities within the material ($\lambda_{us} >> l_{inhomogeneity}$).[45] For this equation to be valid in the LCO battery, the wavelength must be significantly larger than the thickness of a single electrode layer (~50 μm). Based on the material properties of the LCO and graphite, the minimum wavelength of the ultrasonic wave produced by the 2.5-MHz transducers is ~1,000 μm.[32] Therefore, Equation 2 is valid for this system. In addition, note that the term "effective modulus" is used because these experiments measure the effective ultrasonic velocity through the battery,

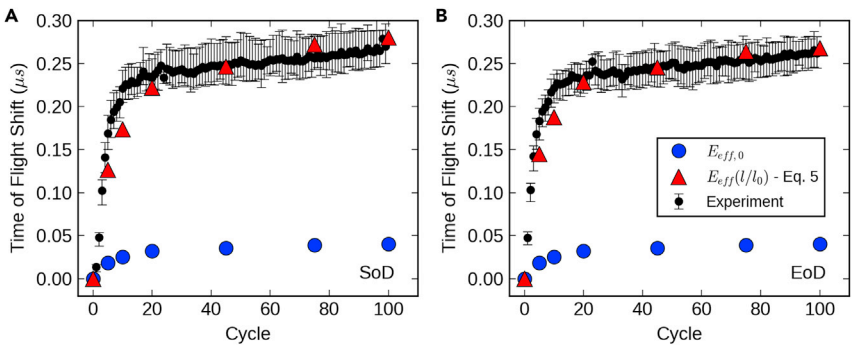

Figure 4. Comparison of Experimental and Calculated ToF Shift

(A) Shift in ultrasonic signal at start of discharge (4.2 V).

(B) Shift in ultrasonic signal at end of discharge (2.7 V).

Experimental data represent the average ToF shift of three cells and the error bars correspond to the spread. All cells were cycled at a C/2 rate between 2.7 and 4.2 V with a constant-voltage charge step at 4.2 V to a C/10 cutoff current. Blue circles correspond to ToF shifts calculated using the thickness data and a constant E_{eff} value (Equation 4). Red triangles correspond to ToF shifts calculated using an E_{eff} value that was dependent on the change in battery thickness (Equation 5).

which depends on the elastic properties of the materials and Backus layering effects.[46] Combining Equations 1 and 2 results in

$$t_{wave} = \left(\frac{ml}{AE_{eff}}\right)^{0.5}. \qquad \text{(Equation 3)}$$

This formulation suggests that the time it takes an ultrasonic wave to traverse the battery is proportional to the square root of its length. Using Equation 3, the expected ToF shift due to thickness change is given as follows:

$$t_{shift} = \left(\frac{m}{A}\right)^{0.5}\left[\left(\frac{l_0}{E_{eff,0}}\right)^{0.5} - \left(\frac{l}{E_{eff}}\right)^{0.5}\right], \qquad \text{(Equation 4)}$$

where l_0 refers to the thickness at cycle 0.

To test whether Equation 4 describes the relationship between the ToF shift and thickness data, we used the average cell thickness data from Figure 3 as input into Equation 4 and compared the results of the calculation with experimental, ultrasonic ToF data. As a first pass, we assumed the effective modulus of the battery was constant for a given state of charge during cycling ($E_{eff,0} = E_{eff}$) and calculated a unique modulus at SoD and EoD.

$E_{eff,0}$ was calculated using Equation 3 along with the first arrival time of the ultrasonic wave at cycle 0 and the mass and area of the active region of the battery (i.e., region of the pouch cell containing electrodes and separators) to approximate the density of the material between the transducers. The mass and area used in the calculations were 4.46 g and 3.45 cm^2, respectively. For calculations at SoD, the initial, average thickness of the batteries at 4.2 V was 6.04 mm and the average first arrival time was 3.755 s, corresponding to an $E_{eff,0,SoD}$ of 5.54 GPa. For calculations at EoD, the initial, average thickness of the batteries at 2.7 V was 5.84 mm and the average first arrival time was 3.85 s, corresponding to an $E_{eff,0,EoD}$ of 5.09 GPa.

A comparison of the calculated and experimental ToF shift is shown in Figure 4, where the blue circles represent the data calculated using Equation 4. Experimental data represent the average ToF shift obtained from three cells and error bars

represent the spread. All shifts are shown in reference to the same state of charge at cycle 0.

Clearly, thickness alone cannot explain the overall increase in the ToF shift, as observed by the severe underprediction of the experimental ToF shift. This suggests that, along with swelling, the effective modulus of the battery is decreasing during cycling. To explain the further increases in ToF shift, we hypothesize that the mechanism responsible for the expansion of the battery is also decreasing the effective modulus. If this is correct, the extent to which this mechanism has occurred inside the battery can be approximated from the total change in cell thickness. Therefore, the influence of the mechanism on the effective modulus can be accounted for indirectly by relating changes in effective modulus directly to changes in the cell thickness.

To test this hypothesis, we assumed E_{eff} to depend on the increase in cell thickness according to the following relationship:

$$E_{eff} = E_{eff,0} + k_E\left(\frac{l}{l_0}\right), \qquad \text{(Equation 5)}$$

where k_E is a constant. The constant k_E provides the linkage between the thickness change (used to quantify the extent of the mechanism) and changes in the effective modulus. Its physical significance will be discussed later in this section.

The expected ToF shift was recalculated using Equation 5 at SoD and EoD with $k_{E,\mathrm{SoD}}$ equal to −3.98 GPa and $k_{E,\mathrm{EoD}}$ equal to −3.00 GPa, respectively. The results of the calculations are shown as the red triangles in Figure 4. Good agreement is observed at both SoD and EoD, suggesting that both battery swelling and decreases in the effective modulus are responsible for the ToF increase.

Because the swelling of the battery is attributed to expansion of the graphite anode,[17,18] it is highly likely that the changes in the graphite anode are also responsible for the decrease in the effective modulus of the battery. This could result from two main mechanisms: (1) the intrinsic moduli of the materials constituting the graphite anode are decreasing, or (2) macroscopic changes in the electrode structure could slow ultrasonic wave propagation. For the first mechanism, intrinsic changes in the moduli could occur through the formation of surface layers on the graphite (often referred to as the solid electrolyte interphase) or through changes to the graphite itself due to exfoliation or irreversible lithium incorporation.[47,48] For the second mechanism, macroscopic changes to the structure of the graphite anode could occur from side reactions that produce surface layers or generate gas within the electrode.[49,50] These changes could slow the ultrasonic wave propagation by decreasing the packing density and increasing the porosity of the electrodes.[51]

To test which of these is the major cause of the ToF shift, we repeated the cycling/EIS experiments using a holder that kept the transducers a fixed distance apart, as opposed to the previous setup that allowed for fluctuations in distance by affixing the transducers to the battery using springs. If changes in the intrinsic moduli of the anode materials are the main cause of the shift, the ToF should still increase during the new experiments. If the impact on the macrostructure of the cell is the main cause, the new experiments should keep the components of the cell compressed together, preventing an increase in ToF with cycling.

Figure S7 shows the R_{CT} and ToF shift for the battery with fixed transducers. First, the trend in R_{CT} is similar to that in the previous cells, as observed in Figure S7A. This

indicates that the constraining of the cell does not affect the electrochemistry. Second, Figure S7B shows that the ToF shift is decreasing with cycling, which indicates that constraining the battery is making it easier for the sound wave to traverse the battery with cycling. This occurs because as the battery swells during cycling, the constrained geometry forces the internal stresses within the cell to increase. The increased internal stresses likely prevent the cell from structural rearrangement caused by graphite anode expansion. This result points to the second hypothesis that, for the base-case with non-stationary transducers, the graphite anode is swelling the battery and causing macroscopic changes to the overall structure, which slows the traversing sound wave.

Furthermore, these results indicate that k_E in Equation 5 describes the extent to which macroscopic changes in the overall structure affect the ability of the sound wave to traverse the battery. Its negative value indicates that structural changes are "slowing down" the sound wave. One likely cause is reduced particle-to-particle contact between the various components of the electrode as it expands.

Additionally, the rapid change in properties at the beginning of cycling also correlates to a rapid decrease in the cell capacity according to Figure S8. Capacity decrease is often attributed to the formation of surface layers, which consumes active lithium and releases gas.[52–54] Therefore, the macroscopic changes in the graphite anode are likely linked to surface layer formation. This conclusion implies that the observed changes in ToF shift during break-in can be used to indicate the extent of surface layer formation occurring within the battery. Such an indicator may help predict the future lifetime of the battery, since the evolution of surface layers is one of the major causes of capacity decay in Li-ion batteries.[34] Furthermore, note that LCO batteries from separate manufacturers do not have similar capacity fades (Figure S8), even though they show similar trends in ToF shift (Figure S4). This could indicate that ToF shift is providing information about the degree of surface layer formation that cannot be obtained from capacity fade alone.

To summarize, the R_{CT} and ToF data indicate that two phenomena are occurring during the break-in period: (1) the active surface area of the LCO is increasing and (2) expansion of the anode is causing the battery to swell, which also affects the effective modulus. The question to be answered is whether or not these behaviors are coupled.

Cycling at Different Voltage Windows Proves Coupling of R_{CT} and ToF Shift

In LCO pouch cells, side reactions continually occur on the anode during cycling because the expansion and contraction of the graphite during lithiation and delithiation, respectively, cause existing surface layers and graphite particles to fracture, which expose fresh graphite to further side reactions and gassing.[44,49,50] This information suggests that the amount of side reactions and, subsequently, the amount of anode swelling during cycling can be controlled by varying the total amount of (de) lithiation into the anode. Therefore, if the EIS and ultrasonic data are coupled, both of these datasets should reflect correlations as a function of (de)lithiation of the graphite during cycling.

To test this hypothesis, we cycled LCO pouch cells between different voltage windows to alter the state of charge of the graphite anode. An overview of the six tests is shown in Table 1, which provides (1) the voltage window used for cycling, (2) the state of charge (SOC) range calculated for each experiment assuming a nominal capacity of 210 mAh, and (3) an estimated percent volume change in the graphite

Table 1. Description of SOC Experiments

Voltage Window (V)	SOC Range (%)	Graphite Volume Change (%)
2.7–3.65	0–5	0.5
2.7–3.9	0–70	6.8
2.7–4.2	0–100	10.0
3.25–4.2	5–100	9.4
3.65–4.2	30–100	6.5
3.9–4.2	80–100	2.0

Estimated, intra-cycle volume change of graphite particles was calculated using data from Qi et al.[55]

particles within a given cycle due to lithiation. The volume change was estimated using the calculated layer spacing of neighboring carbon planes in graphite, LiC_{18}, LiC_{12}, and LiC_6 from Qi et al.[55] Details of the volume estimation can be found in Table S1.

Figure 5 shows the ultrasonic ToF shifts and the change in charge transfer resistance for the experiments in Table 1. Figures 5A and 5C contain data taken at the EoD (after the cells reached 2.7 V) for all tests run with the bottom cutoff voltage of 2.7 V. Figures 5B and 5D contain data taken at the SoD (after the cells were held at 4.2 V) for all tests run with the top cutoff voltage of 4.2 V. There are obvious trends in the ToF and charge transfer resistance as the voltage/SOC window increases (i.e., as the intra-cycle change in graphite volume increases). Namely, larger SOC windows during cycling correspond to increases in the ToF (Figures 5A and 5B) and decreases in the charge transfer resistance (Figures 5C and 5D).

The correlations between increasing SOC window, increasing ToF shift, and decreasing charge transfer resistance are most pronounced for the low cutoff voltage data (Figures 5A and 5C). For the smallest voltage window where graphite is estimated to expand and contract by 0.5%, the ToF decreases slightly and the charge transfer resistance increases to 110% of its original value over the first 50 cycles. In contrast, for the largest voltage window where graphite is estimated to expand and contract by 10%, the ToF increases by 60 ns and the charge transfer resistance decreases to 40% of its original value over the first 50 cycles. Similar trends are observed for the high voltage cutoff data in Figures 5B and 5D, confirming that the trends in ultrasonic and EIS data are coupled.

To better elucidate these trends, Figure 6 plots the ToF shift (Figure 6A) and change in charge transfer resistance (Figure 6B) at cycle 12 (observed end of break-in) for all experiments run in Table 1. The data are plotted with respect to the estimated, intra-cycle change in graphite volume. The solid symbols refer to data taken at EoD (i.e., data from Figures 5A and 5C), while the open symbols refer to data taken at SoD (i.e., data from Figures 5B and 5D). Figure 6 clearly shows that increases in the expansion of the graphite within a cycle (controlled by increasing the SOC window) directly correlate with increases in the ToF shift and decreases in the charge transfer resistance. In addition, the correlation between graphite expansion and ToF shift in Figure 6A supports the claim that increased expansion of the graphite within a cycle will increase side reactions likely responsible for the ToF shift.

Break-In Phenomenon Reflects Non-chemical Crosstalk between Electrodes

The results above suggest that expansion of the graphite anode (likely caused by side reactions resulting in surface layer formation and gassing) has a direct impact

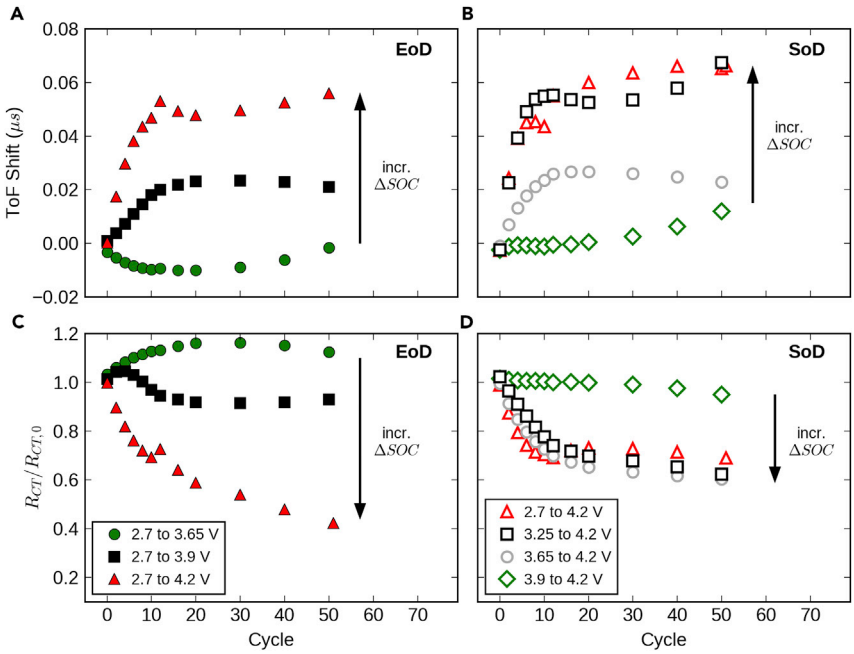

Figure 5. Coupled Behavior of R_{CT}, ToF Shift, and Cycled SOC Window

(A–D) ToF shift of ultrasonic signal for LCO pouch cells cycled between different voltage cutoffs (A and B). ToF shift is reported in reference to the signal obtained at the same SOC at cycle 0 of the experiment. Change in charge transfer resistance of same cells (C and D). (A) and (C) show data at end of discharge (EoD) for cells cycled with a bottom cutoff voltage of 2.7 V. (B) and (D) show data at start of discharge (SoD) for cells cycled with a top cutoff voltage of 4.2 V.

on decreasing the charge transfer resistance of the LCO cathode. To explain this behavior, we hypothesize that expansion of the graphite anode is forcing electrolyte to wet previously inaccessible regions in the LCO cathode. A schematic of this idea is depicted in Figure 7. Figure 7A shows a cell of the battery at cycle 0, where the white space between the particles of the LCO represents the unwetted portion of the electrode. As the cell is cycled (Figure 7B), the graphite electrodes expand (denoted by a black expansion layer), which increases the stack pressure within the cell.[23,24] The increased pressure provides a driving force to move electrolyte around the system, causing the electrolyte to flood the positive electrode and fully wet the LCO particles.

For this hypothesis to be plausible, the LCO electrode must contain a distribution of pore sizes, whereby smaller pores would cause incomplete wetting of the electrode due to high surface tension within the pore. To verify that the tested electrodes meet this criterion, we conducted mercury intrusion porosimetry (MIP) on fresh LCO electrodes, the results of which are shown in Figure S9. MIP shows a distribution of pore diameters from ~20 nm to ~5 μm, with pores larger than 180 nm accounting for 50% of the electrode surface area, indicating that the hypothesis is plausible.

Note that, along with the wetting hypothesis, increases in surface area could result from cracking and fracturing of the electrode particles. To verify that this was not the case, we took scanning electron microscopic images of battery electrodes cycled to 0, 5, 10, and 20 cycles. Representative images at cycles 0 and 20 are shown in Figure S10. No obvious changes in the extent of cracking were observed over all images

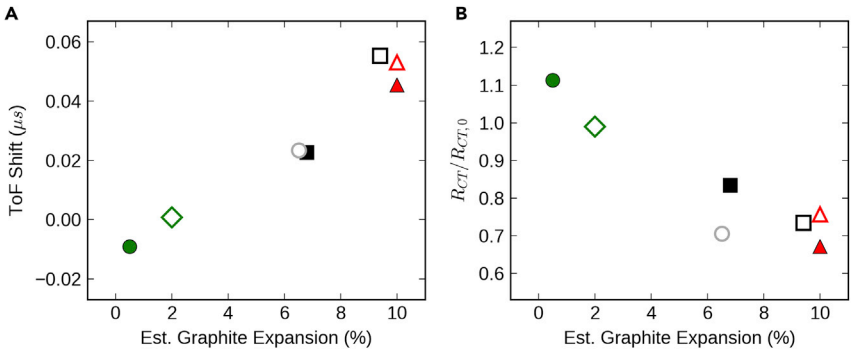

Figure 6. Correlating Intra-cycle Graphite Expansion with R_{CT} and ToF Shift

(A) ToF shift of ultrasonic signal at cycle 12 for LCO pouch cells as a function of estimated graphite expansion. Estimated graphite expansion is taken as the volumetric change in graphite particles from the end of discharge (EoD) to the start of discharge (SoD) (see Tables 1 and S1 for estimation). Symbols correspond to legend in Figure 5.

(B) Change in charge transfer resistance at cycle 12 for the same cells.

at all cycling conditions. In addition, complete fracturing of particles during cycling would result in a larger amount of smaller crystals. To test whether this is occurring, we recorded the particle density and average particle size of the battery electrodes, the results of which are shown in Figure S11. For both electrodes there is no appreciable change in either parameters, further indicating electrolyte wetting as the likely cause of the surface area increases.

The phenomenon outlined herein depicts a non-chemical form of crosstalk between the two electrodes. Previously, the term "crosstalk" has been used exclusively to describe the unwanted diffusion of chemical species between the electrodes, typically from cathode to anode—for example, the diffusion of soluble polysulfides in lithium-sulfur batteries or soluble manganese in lithium-ion batteries employing manganese oxide cathodes.[56,57] In this work we have demonstrated that, even without an exchange of chemical components, crosstalk can still exist and the performances of the anode and cathode are still interdependent.

Conclusions

The break-in period of an LCO/graphite pouch cell corresponds to abrupt changes in the electrochemical impedance and ultrasonic signal through the battery during the first 12 cycles, followed by a gradual plateauing to more constant values. The dominant change in the cell impedance was a decrease in the charge transfer resistance. This was attributed to an increase in the active surface area of the LCO cathode. For the ultrasonic measurements, the break-in period corresponded to an increase in the ToF required for the ultrasonic signal to traverse the battery. This was attributed to growth of the graphite anode, which increased the thickness of the battery and lowered the effective modulus.

The decrease in charge transfer resistance and the increase in ToF shift were both shown to depend on the voltage window used to cycle the battery. It was suggested that the voltage window had a direct impact on graphite particle expansion/contraction, which affected the ultrasonic signal and the impedance measurements. To explain the coupled behavior between the ultrasonics and impedance, we hypothesized that expansion of the graphite electrode (likely caused by side reactions resulting in surface layer formation and gassing) displaces electrolyte in the anode, which

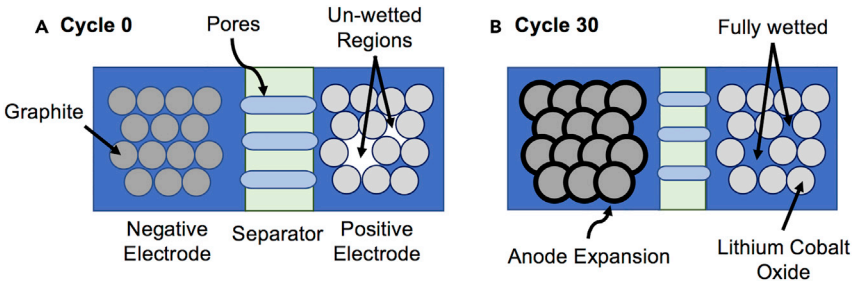

Figure 7. Schematic of the Proposed Electrolyte Wetting Process

(A) Cycle 0 for a single cell: negative electrode (graphite), separator, and positive electrode (lithium cobalt oxide).

(B) Cell at cycle 30.

During cycling, expansion of the graphite electrode displaces electrolyte within the cell, which increases the internal stress and causes electrolyte to wet previously inaccessible portions of the LCO.

increases the internal stress within the battery and forces electrolyte to wet previously inaccessible pores of the LCO cathode.

EXPERIMENTAL PROCEDURES

Simultaneous electrochemical and ultrasonic tests were conducted using commercial lithium-ion battery pouch cells (graphite negative electrode, LCO positive electrode) with a nominal capacity of 210 mAh. Cells were cycled using an Ivium potentiostat at a C/2 rate using a constant-current, constant-voltage (CCCV) charge protocol with a C/20 cutoff current on charge. While cycling, EIS measurements were taken at the top and bottom of charge for various cycles.

For all experiments, the cell was placed inside a custom-built holder and ultrasonic snapshots across the face of the battery were taken every 5 minutes, simultaneously with the cycling and EIS. A schematic and picture of the setup are shown in Figure S1. For each ultrasonic snapshot, the shift in the ToF of the signal through the battery was determined using an in-house algorithm (see Figure 2 in Davies et al.[32] and subsequent discussion).

Along with the EIS/ultrasonic studies, three LCO pouch cells were cycled using a Neware BTS3000 battery cycler with a CCCV protocol and a C/10 cutoff current on charge (cycler's low limit). The full-cell thicknesses were measured periodically using a digital micrometer. In addition, ultrasonic data were obtained under the same conditions by cycling three separate batteries while taking simultaneous ultrasonic snapshots. Both tests were done in triplicate (total of six batteries) to ensure reproducibility of the results. Additional detail and justification for all procedures can be found in Supplemental Experimental Procedures.

SUPPLEMENTAL INFORMATION

Supplemental Information includes Supplemental Experimental Procedures, 11 figures, and 1 table and can be found with this article online at https://doi.org/10.1016/j.joule.2018.03.016.

ACKNOWLEDGMENTS

This work was supported by grants from DOE (APRA-E DE-AR000621) and ExxonMobil as a Charter Member of the Princeton E-filliates Partnership of the

Andlinger Center for Energy and the Environment. The authors thank Andrew Kim, Shaurjo Biswas, and Abhi Raj for useful discussions.

AUTHOR CONTRIBUTIONS

K.W.K., T.H., and D.A.S. developed the idea and drew conclusions from data. G.D. and A.K. provided analysis of the ultrasonic signals. C.B., K.W.K., and T.H. conducted experiments. K.W.K. and T.H. wrote the manuscript.

DECLARATION OF INTERESTS

D.A.S. is a founder of Feasible, which employs the ultrasonic technique (patent application #20160223498) used herein. Feasible did not fund the work nor participate in its execution.

Received: January 7, 2018
Revised: March 20, 2018
Accepted: March 26, 2018
Published: April 18, 2018

REFERENCES

1. Schuster, S.F., Brand, M.J., Berg, P., Gleissenberger, M., and Jossen, A. (2015). Lithium-ion cell-to-cell variation during battery electric vehicle operation. J. Power Sourc. *297*, 242–251.
2. Paul, S., Diegelmann, C., Kabza, H., and Tillmetz, W. (2013). Analysis of ageing inhomogeneities in lithium-ion battery systems. J. Power Sourc. *239*, 642–650.
3. Park, J.I., Baek, S.H., Jeong, M.K., and Bae, S.J. (2009). Dual features functional support vector machines for fault detection of rechargeable batteries. IEEE Trans. Syst. Man Cybernet. C *39*, 480–485.
4. Eom, S.-W., Kim, M.-K., Kim, I.-J., Moon, S.-I., Sun, Y.-K., and Kim, H.-S. (2007). Life prediction and reliability assessment of lithium secondary batteries. J. Power Sourc. *174*, 954–958.
5. Baumhöfer, T., Brühl, M., Rothgang, S., and Sauer, D.U. (2014). Production caused variation in capacity aging trend and correlation to initial cell performance. J. Power Sourc. *247*, 332–338.
6. Harris, S.J., Harris, D.J., and Li, C. (2017). Failure statistics for commercial lithium ion batteries: a study of 24 pouch cells. J. Power Sourc. *342*, 589–597.
7. Han, X., Ouyang, M., Lu, L., Li, J., Zheng, Y., and Li, Z. (2014). A comparative study of commercial lithium ion battery cycle life in electrical vehicle: aging mechanism identification. J. Power Sourc. *251*, 38–54.
8. Remmlinger, J., Buchholz, M., Meiler, M., Bernreuter, P., and Dietmayer, K. (2011). State-of-health monitoring of lithium-ion batteries in electric vehicles by on-board internal resistance estimation. J. Power Sourc. *196*, 5357–5363.
9. Remmlinger, J., Buchholz, M., Soczka-Guth, T., and Dietmayer, K. (2013). On-board state-of-health monitoring of lithium-ion batteries using linear parameter-varying models. J. Power Sourc. *239*, 689–695.
10. Huet, F. (1998). A review of impedance measurements for determination of the state-of-charge or state-of-health of secondary batteries. J. Power Sourc. *70*, 59–69.
11. Maher, K., and Yazami, R. (2014). A study of lithium ion batteries cycle aging by thermodynamics techniques. J. Power Sourc. *247*, 527–533.
12. Zhang, D., Haran, B.S., Durairajan, A., White, R.E., Podrazhansky, Y., and Popov, B.N. (2000). Studies on capacity fade of lithium-ion batteries. J. Power Sourc. *91*, 122–129.
13. Asakura, K., Shimomura, M., and Shodai, T. (2003). Study of life evaluation methods for Li-ion batteries for backup applications. J. Power Sourc. *119–121*, 902–905.
14. Mukoyama, D., Momma, T., Nara, H., and Osaka, T. (2012). Electrochemical impedance analysis on degradation of commercially available lithium ion battery during charge-discharge cycling. Chem. Lett. *41*, 444–446.
15. Waag, W., Käbitz, S., and Sauer, D.U. (2013). Experimental investigation of the lithium-ion battery impedance characteristic at various conditions and aging states and its influence on the application. Appl. Energy *102*, 885–897.
16. Schuster, S.F., Brand, M.J., Campestrini, C., Gleissenberger, M., and Jossen, A. (2016). Correlation between capacity and impedance of lithium-ion cells during calendar and cycle life. J. Power Sourc. *305*, 191–199.
17. Liu, D., Wang, Y., Xie, Y., He, L., Chen, J., Wu, K., Xu, R., and Gao, Y. (2013). On the stress characteristics of graphite anode in commercial pouch lithium-ion battery. J. Power Sourc. *232*, 29–33.
18. Lee, J.H., Lee, H.M., and Ahn, S. (2003). Battery dimensional changes occurring during charge/discharge cycles—thin rectangular lithium ion and polymer cells. J. Power Sourc. *119*, 833–837.
19. Zhang, N., and Tang, H. (2012). Dissecting anode swelling in commercial lithium-ion batteries. J. Power Sourc. *218*, 52–55.
20. Oh, K.-Y., Siegel, J.B., Secondo, L., Kim, S.U., Samad, N.A., Qin, J., Anderson, D., Garikipati, K., Knobloch, A., Epureanu, B.I., et al. (2014). Rate dependence of swelling in lithium-ion cells. J. Power Sourc. *267*, 197–202.
21. Siegel, J.B., Stefanopoulou, A.G., Hagans, P., Ding, Y., and Gorsich, D. (2013). Expansion of lithium ion pouch cell batteries: observations from neutron imaging. J. Electrochem. Soc. *160*, A1031–A1038.
22. Qi, Y., and Harris, S.J. (2010). In situ observation of strains during lithiation of a graphite electrode. J. Electrochem. Soc. *157*, A741–A747.
23. Liu, X.M., and Arnold, C.B. (2016). Effects of cycling ranges on stress and capacity fade in lithium-ion pouch cells. J. Electrochem. Soc. *163*, A2501–A2507.
24. Cannarella, J., and Arnold, C.B. (2014). Stress evolution and capacity fade in constrained lithium-ion pouch cells. J. Power Sourc. *245*, 745–751.
25. Cannarella, J., and Arnold, C.B. (2014). State of health and charge measurements in lithium-ion batteries using mechanical stress. J. Power Sourc. *269*, 7–14.
26. Schiffer, Z.J., Cannarella, J., and Arnold, C.B. (2016). Strain derivatives for practical charge rate characterization of lithium ion electrodes. J. Electrochem. Soc. *163*, A427–A433.
27. Mohan, S., Kim, Y., Siegel, J.B., Samad, N.A., and Stefanopoulou, A.G. (2014). A phenomenological model of bulk force in a Li-ion battery pack and its application to state of charge estimation. J. Electrochem. Soc. *161*, A2222–A2231.
28. Samad, N.A., Kim, Y., Siegel, J.B., and Stefanopoulou, A.G. (2016). Battery capacity fading estimation using a force-based

incremental capacity analysis. J. Electrochem. Soc. *163*, A1584–A1594.

29. Hsieh, A.G., Bhadra, S., Hertzberg, B.J., Gjeltema, P.J., Goy, A., Fleischer, J.W., and Steingart, D.A. (2015). Electrochemical-acoustic time of flight: in operando correlation of physical dynamics with battery charge and health. Energy Environ. Sci. *8*, 1569–1577.

30. Bhadra, S., Hsieh, A.G., Wang, M.J., Hertzberg, B.J., and Steingart, D.A. (2016). Anode characterization in zinc-manganese dioxide AA alkaline batteries using electrochemical-acoustic time-of-flight analysis. J. Electrochem. Soc. *163*, A1050–A1056.

31. Gold, L., Bach, T., Virsik, W., Schmitt, A., Müller, J., Staab, T.E.M., and Sextl, G. (2017). Probing lithium-ion batteries' state-of-charge using ultrasonic transmission—concept and laboratory testing. J. Power Sourc. *343*, 536–544.

32. Davies, G., Knehr, K.W., Van Tassell, B., Hodson, T., Biswas, S., Hsieh, A.G., and Steingart, D.A. (2017). State of charge and state of health estimation using electrochemical acoustic time of flight analysis. J. Electrochem. Soc. *164*, A2746–A2755.

33. Zhang, S.S., Xu, K., and Jow, T.R. (2004). Electrochemical impedance study on the low temperature of Li-ion batteries. Electrochim. Acta *49*, 1057–1061.

34. Vetter, J., Novák, P., Wagner, M.R., Veit, C., Möller, K.-C., Besenhard, J.O., Winter, M., Wohlfahrt-Mehrens, M., Vogler, C., and Hammouche, A. (2005). Ageing mechanisms in lithium-ion batteries. J. Power Sourc. *147*, 269–281.

35. Osaka, T., Momma, T., Mukoyama, D., and Nara, H. (2012). Proposal of novel equivalent circuit for electrochemical impedance analysis of commercially available lithium ion battery. J. Power Sourc. *205*, 483–486.

36. Osaka, T., Nakade, S., Rajamäki, M., and Momma, T. (2003). Influence of capacity fading on commercial lithium-ion battery impedance. J. Power Sourc. *119–121*, 929–933.

37. Momma, T., Matsunaga, M., Mukoyama, D., and Osaka, T. (2012). Ac impedance analysis of lithium ion battery under temperature control. J. Power Sourc. *216*, 304–307.

38. Wu, Q., Lu, W., and Prakash, J. (2000). Characterization of a commercial size cylindrical Li-ion cell with a reference electrode. J. Power Sourc. *88*, 237–242.

39. Nagasubramanian, G. (2000). Two- and three-electrode impedance studies on 18650 Li-ion cells. J. Power Sourc. *87*, 226–229.

40. Ratnakumar, B.V., Smart, M.C., and Surampudi, S. (2002). Electrochemical impedance spectroscopy and its applications to lithium ion cells. In Seventeenth Annual Battery Conference on Applications and Advances. Proceedings of Conference (Cat. No. 02TH8576), pp. 273–277.

41. Wu, M.-S., Chiang, P.-C.J., and Lin, J.-C. (2005). Electrochemical investigations on advanced lithium-ion batteries by three-electrode measurements. J. Electrochem. Soc. *152*, A47–A52.

42. Barker, J., Pynenburg, R., Koksbang, R., and Saidi, M.Y. (1996). An electrochemical investigation into the lithium insertion properties of Li_xCoO_2. Electrochim. Acta *41*, 2481–2488.

43. Dokko, K., Mohamedi, M., Fujita, Y., Itoh, T., Nishizawa, M., Umeda, M., and Uchida, I. (2001). Kinetic characterization of single particles of $LiCoO_2$ by AC impedance and potential step methods. J. Electrochem. Soc. *148*, A422–A426.

44. Broussely, M., Biensan, P., Bonhomme, F., Blanchard, P., Herreyre, S., Nechev, K., and Staniewicz, R.J. (2005). Main aging mechanisms in Li ion batteries. J. Power Sourc. *146*, 90–96.

45. Fjar, E., Holt, R.M., Raaen, A.M., Risnes, R., and Horsrud, P. (2008). Petroleum Related Rock Mechanics (Elsevier).

46. Backus, G.E. (1962). Long-wave elastic anisotropy produced by horizontal layering. J. Geophys. Res. *67*, 4427–4440.

47. Pinson, M.B., and Bazant, M.Z. (2013). Theory of SEI formation in rechargeable batteries: capacity fade, accelerated aging and lifetime prediction. J. Electrochem. Soc. *160*, A243–A250.

48. Sarasketa-Zabala, E., Aguesse, F., Villarreal, I., Rodriguez-Martinez, L.M., López, C.M., and Kubiak, P. (2015). Understanding lithium inventory loss and sudden performance fade in cylindrical cells during cycling with deep-discharge steps. J. Phys. Chem. C *119*, 896–906.

49. Deshpande, R., Verbrugge, M., Cheng, Y.-T., Wang, J., and Liu, P. (2012). Battery cycle life prediction with coupled chemical degradation and fatigue mechanics. J. Electrochem. Soc. *159*, A1730–A1738.

50. Michalak, B., Sommer, H., Mannes, D., Kaestner, A., Brezesinski, T., and Janek, J. (2015). Gas evolution in operating lithium-ion batteries studied in situ by neutron imaging. Sci. Rep. *5*, 15627.

51. Wyllie, M.R.J., Gregory, A.R., and Gardner, L.W. (1956). Elastic wave velocities in heterogeneous and porous media. Geophysics *21*, 41–70.

52. Verma, P., Maire, P., and Novák, P. (2010). A review of the features and analyses of the solid electrolyte interphase in Li-ion batteries. Electrochim. Acta *55*, 6332–6341.

53. Ein-Eli, Y., Markovsky, B., Aurbach, D., Carmeli, Y., Yamin, H., and Luski, S. (1994). The dependence of the performance of Li-C intercalation anodes for Li-ion secondary batteries on the electrolyte solution composition. Electrochim. Acta *39*, 2559–2569.

54. Liebenow, C., Wagner, M.W., Lühder, K., Lobitz, P., and Besenhard, J.O. (1995). Electrochemical behaviour of coated lithium-carbon electrodes. J. Power Sourc. *54*, 369–372.

55. Qi, Y., Guo, H., Hector, L.G., and Timmons, A. (2010). Threefold increase in the Young's modulus of graphite negative electrode during lithium intercalation. J. Electrochem. Soc. *157*, A558–A566.

56. Bruce, P.G., Freunberger, S.A., Hardwick, L.J., and Tarascon, J.-M. (2011). Li-O_2 and Li-S batteries with high energy storage. Nat. Mater. *11*, 19–29.

57. Schipper, F., Erickson, E.M., Erk, C., Shin, J.-Y., Chesneau, F.F., and Aurbach, D. (2017). Review—recent advances and remaining challenges for lithium ion battery cathodes. J. Electrochem. Soc. *164*, A6220–A6228.